

Received June 4, 2020, accepted June 16, 2020, date of publication June 23, 2020, date of current version July 2, 2020.

Digital Object Identifier 10.1109/ACCESS.2020.3004337

Deep-Learning-Based Predictive Architectures for Self-Piercing Riveting Process

SEHYEOK OH¹, HYUN KYUNG KIM¹, TAEK-EON JEONG², DONG-HYUCK KAM²,
AND HYUNGSON KI¹

¹Department of Mechanical Engineering, Ulsan National Institute of Science and Technology (UNIST), Ulsan 44919, South Korea

²Joining Research and Development Group, Korea Institute of Industrial Technology, Incheon 21999, South Korea

Corresponding author: Hyungson Ki (hski@unist.ac.kr)

This work was supported by the Ministry of Trade, Industry, and Energy, South Korea, through the Industry Core Technology Development Program.

ABSTRACT Deep-learning architectures were developed for the self-piercing riveting (SPR) process to predict the cross-sectional shape from the scalar input of the punch force. Traditionally, the SPR process is studied using a physic-based approach, including finite element modeling, but in this study, a data-driven approach consisting of two supervised deep-learning models was proposed. The first model was used for data transformation from an optical microscopic image to a material segmentation map, which characterizes the shape and location of the two sheets and the rivet by applying a convolutional neural network (CNN)-based deep-learning structure. To validate the developed models, two types of sheet combinations were tested, namely, carbon-fiber-reinforced plastic (CFRP) and galvanized dual-phase steel (GA590DP) sheets, and steel alloy (SPFC590DP) and aluminum alloy (Al5052-H32) sheets. The transformation was performed with a mean intersection-over-union of 98.50% and a mean pixel accuracy of 99.78%. The next model, which was a novel generative model based on a CNN and conditional generative adversarial network with residual blocks, was then trained to predict the cross-sectional shape from the input punch force. The predicted cross-sectional shapes were compared with the experimental results of SPR. The overall accuracy was 94.20% for CFRP-GA590DP and 96.31% for SPFC590DP-Al5052, with respect to three key geometrical indexes, namely, rivet head height, interlock length, and bottom thickness.

INDEX TERMS Cross-sectional shape prediction, deep learning, segmentation prediction, scalar-to-segmentation generator, self-piercing riveting.

I. INTRODUCTION

Self-piercing riveting (SPR) is one of the most promising techniques for joining sheet materials. It is drawing increasing attention, especially in the automotive industry. This is because it can join sheets of similar or dissimilar materials with combinations such as steel–steel, steel–aluminum, and even composite–metal, which are otherwise difficult to join with conventional mechanical machining [1], [2]. A rivet pressed using a punch directly penetrates the top sheet, and the rivet legs at the bottom sheet are flared to fit the die and form a mechanical interlock. Using this technique, two or more sheets can be easily joined in a single step, without requiring a preprocessed hole or thermal deformation.

The associate editor coordinating the review of this manuscript and approving it for publication was Shuihua Wang¹.

To successfully perform SPR, the process must be simulated before actually performing it because the cross-sectional shape after riveting determines the quality of the joint [3]. Porcaro *et al.* [4] simulated the SPR of two aluminum alloy plates based on a two-dimensional axisymmetric model using the finite element method (FEM), and the simulation results for the deformed cross-sectional shape were compared with the experimental data. In addition to the geometrical modeling of the joining process, Casalino *et al.* [5] modeled a physical failure mechanism of the joint in the SPR process for an aluminum alloy by solving the governing equations using FEM and experimentally validating their prediction results. Applying the failure investigation results from [5], Atzeni *et al.* [6] performed SPR of aluminum sheets experimentally and numerically using the FEM, and the deformed shapes were compared. Huang *et al.* [7] conducted FEM-based numerical simulation

of SPR of aluminum alloy and steel sheets with various fracture criteria, and experimentally verified the model in terms of the deformed shape, force–displacement curve, and residual stress profile. Building on the previous FEM simulations, Carandente *et al.* [8] proposed an improved thermomechanical FEM model for various SPR processes, including thermal softening and strain hardening, and conducted experiments on SPR of aluminum sheets to verify the model. The predicted cross-sectional shape was compared with the experimental results. Ma *et al.* [9] numerically investigated the friction SPR of aluminum and magnesium using a three-dimensional thermomechanical-coupled FEM code, and the predicted deformed shape was compared with the experimental result. Hönsch *et al.* [10] performed FEM simulations for SPR of aluminum alloys, and three joint shapes were predicted and compared with the experimental results. Without FEM simulations, Haque *et al.* [11] proposed a rivet flaring model for predicting the amount of rivet displacement from the force–displacement curves and geometries of the sheets, die, and rivet. Di Franco *et al.* [1] performed experiments and FEM simulations for SPR between carbon-fiber-reinforced plastic (CFRP) and aluminum alloy sheets, and the deformed shape was predicted. Moreover, Kroll *et al.* [12] experimentally performed the SPR of CFRP and aluminum alloy sheets by focusing on the fiber orientations and simulated the joint formation using FEM. Hirsch *et al.* [13] simulated the SPR of fiber-reinforced polymers and metal sheets using the FEM. The simulation was based on a damage model to consider the deformation and failure behavior of the composites. Most of the abovementioned studies are based on FEM simulations. They give insights into the process but typically require careful selection of the mesh size and time step and need long computation times.

In this study, a novel deep-learning framework was developed to predict the cross-sectional shape of the SPR joint from the scalar input punch force. Using the proposed deep-learning architecture, we could obtain cross-sectional shapes, including the location and deformed shapes of the rivet and sheets, which influence the quality of SPR joints. The general advantages of using a deep-learning-based predictive model are as follows. a) As the training is based on experimental data without any assumptions (data-driven), prediction results are close to the real ones. b) Even for very complex problems, effective predictions can be made as long as sufficient experimental data are available. c) Compared to conventional FEM simulations, the prediction time is extremely short (within a few seconds) once the training ends. Furthermore, problems associated with meshing and time steps are eliminated.

In this study, the concept of material segmentation was first developed, which classifies the cross-section by material for characterizing the joint shape. To automatize this process using cross-sectional optical microscopic (OM) images, we trained a convolutional neural network (CNN) [14]-based encoder-decoder [15] structured deep-learning model (DeepLabv3+; [16]). The next deep-learning model was designed to predict the

cross-sectional shape (material segmentation map) from an input punch force (a scalar value). This is a novel generative model based on the CNN, called the conditional generative adversarial network (cGAN) [17], [18]; it comprised residual blocks [19], [20], where predictive segmentation images were generated from a scalar value (namely, a scalar-to-seg generator). The second deep-learning architecture was the major predictive model, and the first segmentation model was employed to automatically supply the training data to the second model.

For data preparation, SPR experiments were conducted using two types of sheet combinations, which were CFRP and galvanized dual-phase steel (GA590DP) sheets, and steel alloy (SPFC590DP) and aluminum alloy (Al5052) sheets, by varying the punch force while fixing other process parameters. Using the observed cross-sectional OM images, artificial intelligence (AI) models were trained and validated. The segmentation model, which was trained with the SPR OM image data, segmented the OM images in the test set with a 98.50% mean intersection-over-union (mIOU) and 99.78% mean pixel accuracy (mPA). Furthermore, our segmentation model can segment the SPR OM images regardless of the material combination types (i.e. one trained model can segment both CFRP-GA590DP and SPFC590DP-Al5052 combinations, with the given accuracies). For the cross-section prediction model, which was trained with the material segmentation map, the prediction quality was assessed based on the foremost geometric parameters that determine the joint quality, which were the rivet head height (95.66%, 92.76%), interlock length (90.78%, 97.55%), and bottom thickness (96.16%, 98.60%) (the former: CFRP-GA590DP, the latter: SPFC590DP-Al5052). Mean accuracies were 94.20% and 96.31%, respectively, for the two material combinations.

In summary, the key contributions of this study are as follows.

- We developed a novel deep-learning framework for predicting cross-sectional shapes in SPR processes.
- We introduced the concept of material segmentation to characterize the cross-sectional shapes of rivet and sheets. Correspondingly, a state-of-the-art deep-learning model for image segmentation was introduced along with appropriate hyperparameters.
- We designed a novel scalar-to-segmentation generator by modifying the conventional conditional GAN structure. A simple case study was performed to validate the designed generator.

II. SPR EXPERIMENT

In SPR, there are several process parameters that synthetically affect the joint quality, such as geometrical shapes and dimensions of the rivets, sheets, and dies, material properties, and process parameters such as the punch force and speed [3]. The parameters and the corresponding values used in this study are given in Table. 1 and Fig. 1. Two different types of material combinations were used in the SPR experiment. These were a thermoset CFRP as the top sheet and GA590DP

TABLE 1. SPR process parameters used in this study.

Sheet materials	Location	Tensile strength (MPa)	Thickness (mm)	Coating	Punch force
CFRP	Top	1094 (Y-dir.)	1.3	None	29–70 kN
GA590DP	Bottom	610	2.3	Zn (43.8 g/m ²)	
SPFC590DP	Top	609	1.4	None	28–46 kN
Al5052-H32	Bottom	228	2.0	None	
Rivet	Hardness (HV)	Coating	Blank holder (<i>D</i> : diameter)	Edge distance (mm)	
Boron steel (supplied by BÖLLHOFF)	480 ± 30	Almac® (Al/Zn)	<i>D</i> _{outer} : 13 mm <i>D</i> _{inner} : 8.5 mm Pressure: 52.64 MPa	15	

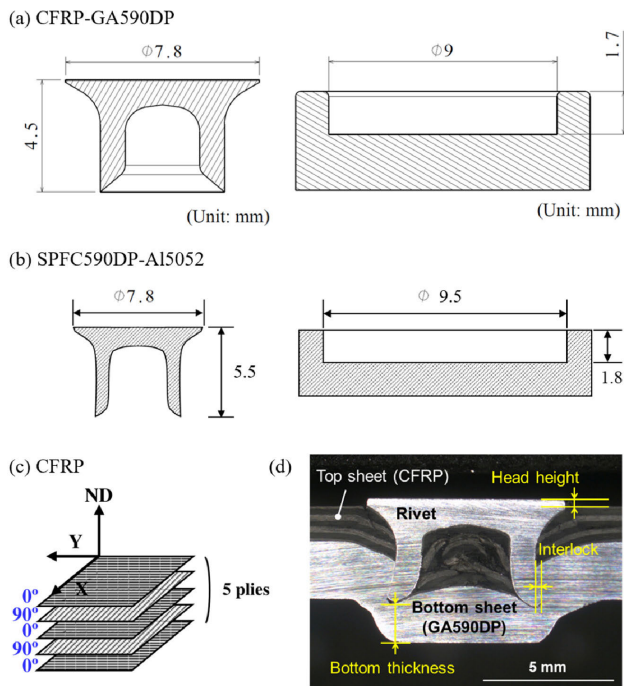


FIGURE 1. Geometrical dimensions of the rivet and die for (a) CFRP-GA590DP and (b) SPFC590DP-Al5052. Laminate sequence of cross-ply composites (0°/90°) and geometrical parameters of the SPR joint are shown in (c) and (d), respectively.

steel as the bottom sheet, and SPFC590DP steel alloy as the top sheet and Al5052-H32 alloy as the bottom sheet. No adhesive or lubricant was used. The CFRP consisted of five cross-ply laminates (0°/90°), as shown in Fig. 1(c). The tensile strength, thickness, coating, and applied punch forces are listed in Table 1 with the rivet and blank holder properties, and the geometrical shapes and dimensions of the rivet and die are shown in Fig. 1(a) (CFRP-GA590DP) and Fig. 1(b) (SPFC590DP-Al5052). As presented in Fig. 1, the die (supplied by BÖLLHOFF) has a basic flat-bottom shape. SPR joints were fabricated using a hydraulic riveting machine (Rivset Gen2, BÖLLHOFF) with a maximum setting force of 78 kN. The punch speed was not varied (it was approximately 0.13 m/s) as the riveting machine was of the hydraulic type.

To assess the prediction quality, three geometrical indexes of the SPR joint were measured, namely, the head height

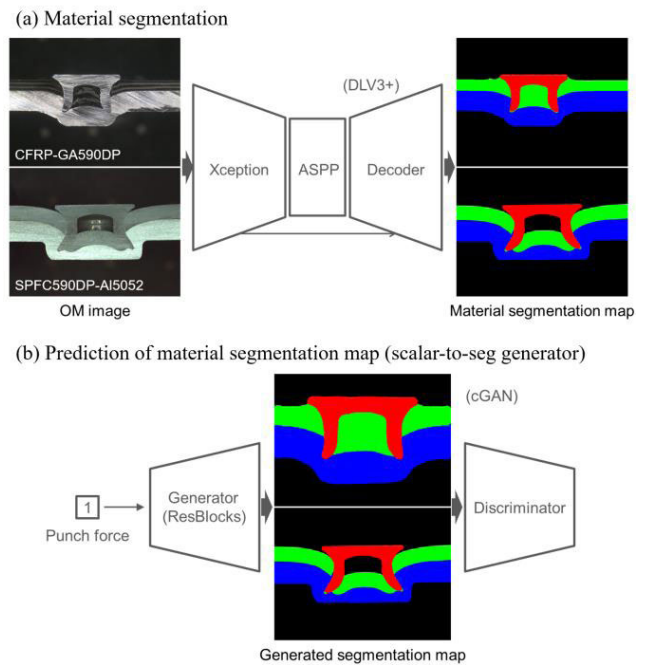


FIGURE 2. Overview of the deep-learning models adopted in this study for (a) material segmentation using OM images and (b) segmentation map prediction using scalar punch forces.

(distance between the rivet head surface and the upper surface of the top sheet), interlock width (distance between the tip of the deformed rivet shank and the pierced point of the top sheet), and bottom thickness (remaining thickness of the bottom sheet after the riveting), as presented in Fig. 1(d). All geometrical indexes were measured twice for every OM image (left and right) and then averaged. For the CFRP-GA590DP, the experiment was conducted with nine different punch forces (29, 34, 39, 44, 49.8, 55, 60, 65, and 70 kN) and repeated thrice for each punch force. For the SPFC590DP-Al5052, seven punch forces (28, 31, 34, 37, 40, 43, and 46 kN) were employed and the process was repeated twice for each punch force.

III. DEEP-LEARNING MODELS

An overview of the employed deep-learning models is presented in Fig. 2.

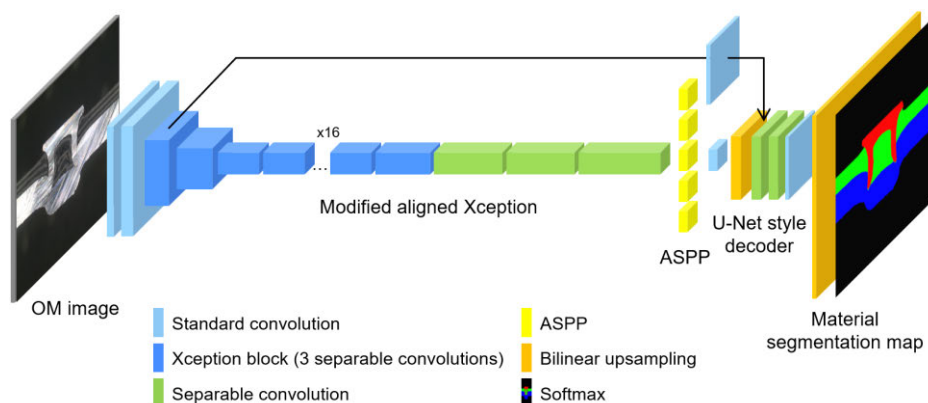


FIGURE 3. Architecture of the segmentation deep-learning model used in this study. The structure is a CNN-based encoder-decoder with atrous separable convolutions.

The concept of image segmentation in computer vision was adopted to characterize the cross-sectional shape of the self-pierced specimen from the OM image. Particularly, the segmentation was conducted material by material (rivet, upper sheet, and lower sheet), as shown in Fig. 2(a). Therefore, the process was named “material segmentation” in this study. In the segmenting process, unnecessary information contained in the OM image, such as surface details, the texture of the materials, image contrast, and noise, was removed, and only essential information such as geometry and location of the materials was retained. The segmented maps were then used as training data in the predictive model instead of the OM images, as shown in Fig. 2(b). In this study, the predictive deep-learning model was the major model, and the segmentation model was the ancillary model, which facilitated data supply to the predictive model (considering the need for further training in the future).

Google’s DeepLabv3+ [16] was employed for the segmentation model, and for the predictive model, a generative model based on the CNN and cGAN architectures with residual blocks was adopted with a modified objective function. All the deep-learning source codes were implemented using Python™ and TensorFlow™. The deep-learning segmentation model is introduced in Section III-A, deep-learning predictive model is introduced in Section III-B, and training information is presented in Section III-C.

A. MATERIAL SEGMENTATION

To prepare the training data from the experimentally obtained cross-sectional OM images, pixel-by-pixel material segmentation was performed manually, including assigning different labels (colors) to different materials. For instance, in the material segmentation map shown in Fig. 2(a), the red, green, blue, and black labels represent the rivet, upper sheet, lower sheet, and background, respectively. The OM image and its segmentation map were used as the input and ground truth, respectively, in the deep-learning segmentation model (DeepLabv3+). In Fig. 3, a schematic architecture of the

model is presented; the figure legend shows the six kinds of operation blocks.

As seen in the figure, a CNN-based encoder-decoder structure was used, where the input SPR OM image was encoded through modified aligned Xception and atrous spatial pyramid pooling modules, and the encoded features were reconstructed into the segmentation map through a U-Net style decoder. In this model, in line with the purpose of image segmentation, a separable convolution that effectively reduces the amount of computation and an atrous convolution that allows the weight filter to process a larger area with the same amount of computation were applied throughout the structure. In addition, Xception [21], which is a powerful deep-learning architecture for image classification, was modified and applied in the encoding line, and the U-Net [22] structure, which concatenates on the encoded features to the decoding line, was utilized. The detailed explanation of the model is not presented in this paper to ensure conciseness; this information can be obtained from another DeepLabv3+ article [16].

B. CROSS-SECTIONAL SHAPE PREDICTION

For the deep-learning predictive model, a generative model based on the CNN and cGAN architectures with residual blocks was designed to predict the material segmentation map from a scalar punch force (namely, scalar-to-seg generator), as shown in Fig. 4. As depicted, the model consisted of two main components: 1) a generator (G) for creating the material segmentation map from the punch force (c ; a scalar value) and a latent variable (z ; a vector); 2) a discriminator (D) for discriminating the generated segmentation map ($G(c, z)$) from the ground truth (x). The random latent variable z was introduced to avoid deterministic mapping, considering that the SPR experiment was repeated multiple times per punch force (i.e., there were three and two OM images per punch force for the CFRP-GA590DP and SPFC590DP-A15052 combinations, respectively). In the cGAN, the latent variable allowed us to obtain slightly different results while maintaining the

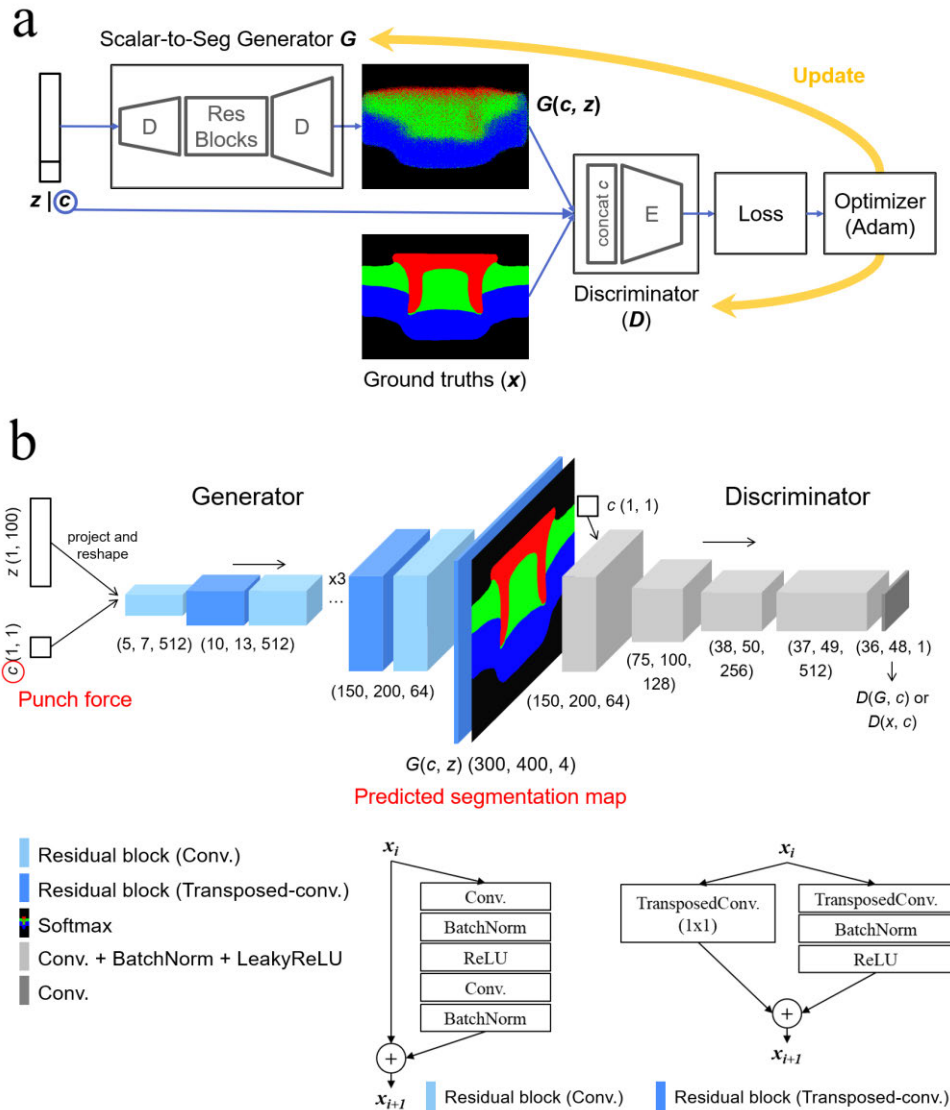


FIGURE 4. Architecture of the generative model (scalar-to-seg generator). It is based on the CNN and cGAN structures with residual blocks. Presented segmentation map and spatial dimensions of the inner layers are for the CFRP-GA590DP material combination.

main characteristics according to the given condition (c), including major geometrical properties, such as the head height, interlock length, and bottom thickness in SPR. The values of z and c were input to the generator after a linear layer, and the number of initial feature maps was set to 465 and 47, respectively. (z : $(N, 100) \rightarrow \text{reshape}(\text{linear}(z))$: $(N, 5, 7, 465)$; c : $(N, 1) \rightarrow \text{reshape}(\text{linear}(c))$: $(N, 5, 7, 47)$; input to the generator $z|c$: $(N, 5, 7, 512)$ (concatenated); N : batch size) The ratio of initial feature maps was approximately 10:1 (465:47) for z and c , which was considered the optimum ratio for our dataset (identified from trial and error).

In Fig. 4, four kinds of convolutional blocks are presented and the numbers below each block denote the shapes of the convoluted images ((H, W, C) , i.e., the number of pixels in the height, width, and channel directions, respectively).

For the CFRP-GA590DP combination, the dimensions of the generated images were $H = 300$ and $W = 400$, as shown in the figure, and for the SPFC590DP-A15052 combination, the dimensions were $H = 245$ and $W = 480$ (accordingly, the shape input to the generator $z|c$ was $(N, 3, 8, 512)$). In Fig. 4, only the results for CFRP-GA590DP are presented for brevity. Inside the generator, considering the large size of the segmentation map (300×400 and 240×480), residual connections [19], [20] were utilized as exhibited by light blue and dark blue blocks in Fig. 4 along with their configurations. Residual connections are widely used for super-resolution problems in computer vision [23]–[27] because they can deepen the layer while maintaining the backpropagation gradients. The residual connection adopted in the light blue block in Fig. 4 is the one [20] used in pix2pixHD [24] and

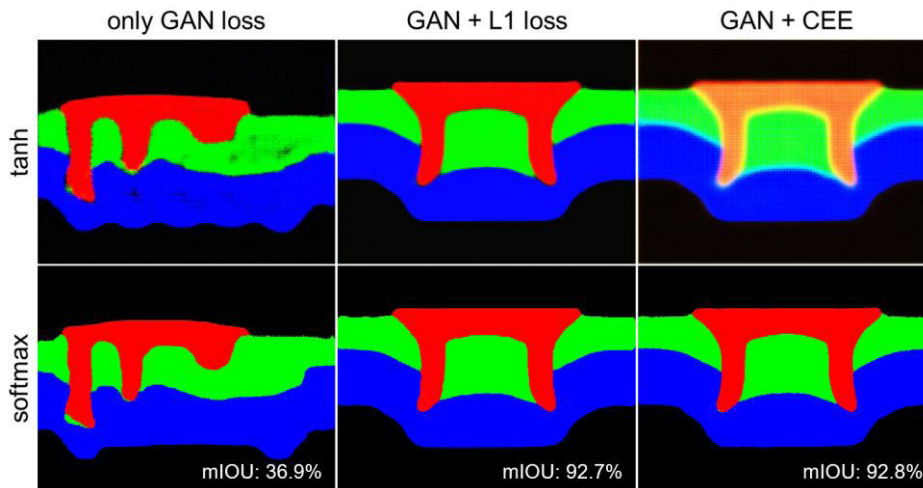


FIGURE 5. Results of the case study. We tested three objective functions (row) and two last activation functions of the generator (column). Tested sheet combination was the CFRP-GA590DP and punch force was 55 kN.

super-resolution GAN [23]. It is composed of two convolutional layers and batch normalization layers [28]. It is worth noting that we also tested instance normalization [29] instead of batch normalization, which is adopted in pix2pixHD. However, we could not improve generation quality. The dark blue residual block in Fig. 4 comprises transposed convolutional layers, which upscale the input image. For an intermediate nonlinear activation of both blocks, a rectified linear unit (ReLU) [30] function was used.

The light and dark gray blocks used in the discriminator constitute a convolution–batch normalization–leaky ReLU ($\max(0.2x, x)$) [31] layer and a single convolutional layer, respectively, following the well-known discriminator structure [32], [33].

Based on the results of previous studies [23], [33], [34] stating that adding a conventional loss function to the GAN loss highly improved the generation quality, we conducted a case study for the objective function, considering the data type as the segmentation map. Accordingly, the last activation function of the generator was also included in the case study and its results are shown in Fig. 5. As observed in the figure, for the traditional loss function, the L1 cost and cross-entropy error (CEE) were tested (L2 was excluded from the case study as it produces a blurrier image than L1 [33]). The generator minimized the added cost function and deceived the discriminator. For the last activation function, hyperbolic tangent (tanh) [32] and softmax were tested. For the GAN loss, we used the least-squares GAN loss (LSGAN; [35]) as it has higher stability than the traditional GAN:

$$\min_D V_D = \frac{1}{2} \mathbb{E}_{x,c} [(D(x, c) - 1)^2] + \frac{1}{2} \mathbb{E}_{c,z} [(D(G(c, z), c))^2], \quad (1)$$

$$\min_G V_G = \frac{1}{2} \mathbb{E}_{c,z} [(D(G(c, z), c) - 1)^2] + \lambda \mathcal{L}(G), \quad (2)$$

$$\mathcal{L}(G) = \mathcal{L}_{L1}(G) = \mathbb{E}_{x,c,z} [\|x - G(c, z)\|_1] \text{ or} \\ \mathcal{L}(G) = \mathcal{L}_{\text{cross entropy}}(G) = \mathbb{E}_{x,c,z} [-x \ln G(c, z)], \quad (3)$$

where V_D and V_G denote the objective functions for the discriminator and generator, respectively, and $\mathcal{L}(G)$ is the to-be-added conventional cost function (L1 or CEE). Further details of the GAN loss can be obtained from [17], [18] and LSGAN papers [35]. As shown in Fig. 5, without the extra loss (i.e. only GAN loss), the generation quality is poor and the generator fails to learn the right mapping between the input (c, z) space and ground truth. When checking the generated images in every epoch with a loss profile, we could confirm that the initial training of the generator was not properly performed; thus, all the training iterations were substantially unstable. However, when trained with the L1 loss (second column in Fig. 5), the generator produced considerably better results, and the last activation of the softmax layer showed much better quality than that of tanh (sharper edges without blurring; mIOU = 92.7%), which actually is an obvious result as the data type was the segmentation map (0 or 1 is allocated in each material class). With the CEE (third column in Fig. 5), the generation result with the softmax layer was significantly better (mIOU = 92.8%) than that with the tanh layer, which showed under-developed generation. In summary, adding the conventional loss function to the GAN cost largely contributed toward initiating the generator training; further, given the type of ground truth (segmentation map), using the softmax layer as the last activation function of the generator proved effective. Moreover, both GAN + L1 and GAN + CEE satisfactorily worked; however, GAN + CEE was adopted in this study, as it showed slightly higher accuracy with clearer material boundaries.

C. TRAINING DETAILS

The material segmentation model was trained on dual TITAN RTX GPUs. Among 41 pairs of [OM, segmentation] data (27 pairs for CFRP-GA590DP and 14 pairs for SPFC590DP-AI5052), 7, 7, and 27 pairs were used for model

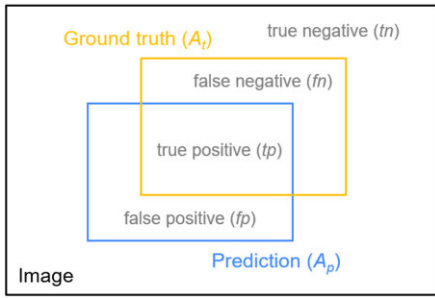


FIGURE 6. Schematic for the image segmentation.

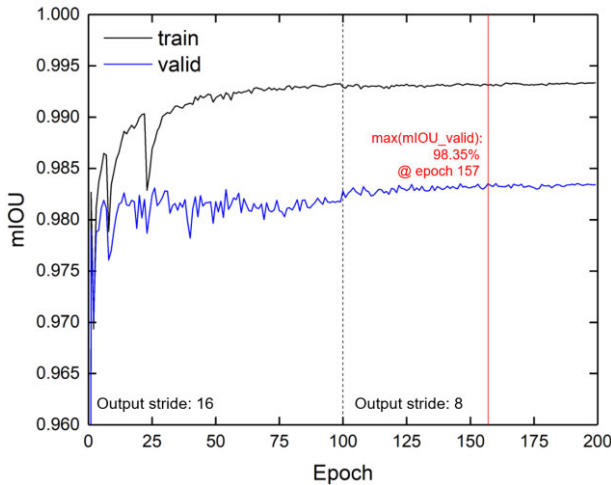


FIGURE 7. mIOU-epoch profile for the training (black) and validation (blue) sets (DeepLabv3+).

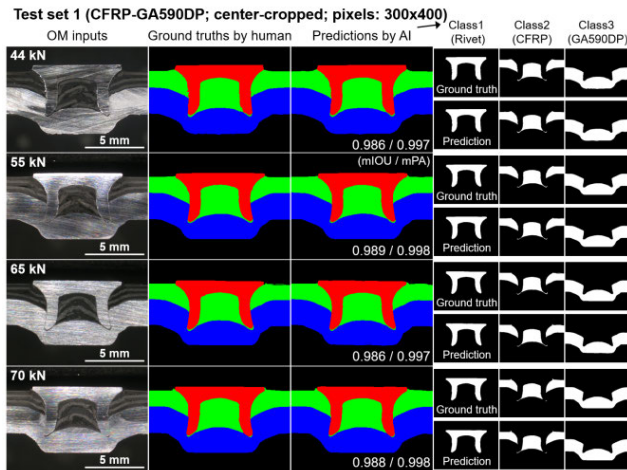


FIGURE 8. Material segmentation results for the first test set. OM inputs, their ground truths, prediction results, and channel-by-channel segmentation results for three material classes are shown in each column from left to right (the background class is omitted).

validation, testing, and training, respectively (randomly chosen). Both the CFRP-GA590DP and SPFC590DP-AI5052 sheet combinations were included in the training dataset to allow the AI model to segment the OM images regardless

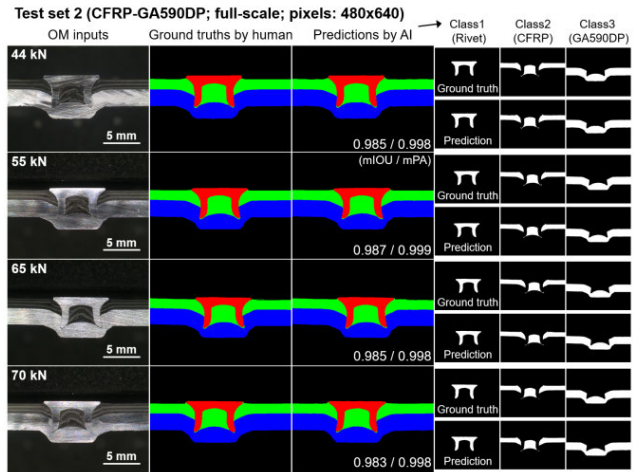


FIGURE 9. Material segmentation results for the second test set. OM inputs, their ground truths, prediction results, and channel-by-channel segmentation results for three material classes are shown in each column from left to right (the background class is omitted).

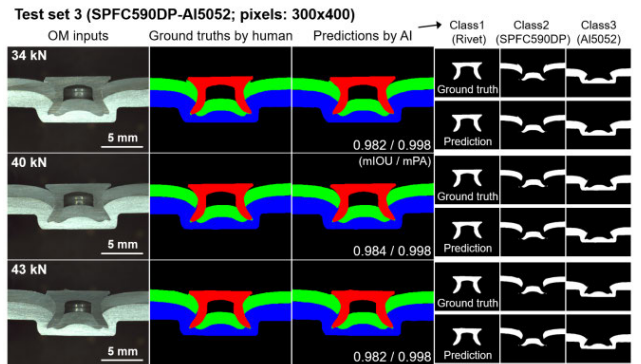


FIGURE 10. Material segmentation results for the third test set. OM inputs, their ground truths, prediction results, and channel-by-channel segmentation results for three material classes are shown in each column from left to right (the background class is omitted).

of the material types. The training data were augmented to 5400 (27×200) in every epoch by applying random cropping, random scaling, and random flipping of the images. The model was trained according to the training protocol of DeepLabv3+, which was a polynomial learning rate policy where the initial learning rate was decayed by $(1 - \text{iteration}/\text{iteration}_{\text{max}})^{\text{power}}$ (power was set to 0.9). Two training sessions were conducted successively. In the first 100 epochs, the initial learning rate was 0.001 with a batch size of 15 and an output stride of 16; in the next 100 epochs, the initial learning rate was 0.0001 with a batch size of five and an output stride of eight. The L2 weight decay coefficient was 10^{-7} . We trained the model from the scratch (no pretraining) and the parameters in the batch norm layers were not frozen even when the output stride was eight. As measures of segmentation performance, the intersection-over-union (IOU) and pixel accuracy (PA) were calculated [36].

TABLE 2. IOU and PA accuracies (%) for the three test sets according to class.

1. CFRP-GA590DP (300 × 400)	Class1 (rivet)	Class2 (CFRP)	Class3 (GA590DP)	Class4 (background)	Mean
IOU	98.20	98.06	99.06	99.54	98.71 (mIOU)
PA	99.77	99.67	99.77	99.79	99.75 (mPA)
2. CFRP-GA590DP (480 × 640)	Class1 (rivet)	Class2 (CFRP)	Class3 (GA590DP)	Class4 (background)	Mean
IOU	97.67	97.87	98.75	99.76	98.51
PA	99.89	99.78	99.81	99.83	99.83
3. SPFC590DP- Al5052 (300 × 400)	Class1 (rivet)	Class2 (SPFC590DP)	Class3 (Al5052)	Class4 (background)	Mean
IOU	97.25	97.41	98.75	99.68	98.28
PA	99.80	99.70	99.82	99.79	99.78
mIOU avg.			-		98.50%
mPA avg.			-		99.78%

In Fig. 6, a schematic showing image segmentation is presented. The blue square is the predicted segmentation area (A_p) and the orange square is the ground truth area (A_t). Note that the area encompassing the predicted values was segregated into “positive” and “negative”; the area encompassing the correct predictions was marked as “true” and that encompassing the incorrect predictions was marked as “false”. From the figure, IOU and PA were calculated as

$$\text{IOU} = \frac{tp}{tp + fp + fn} = \frac{A_p \cap A_t}{A_p \cup A_t}, \quad (4)$$

$$\text{PA} = \frac{tp + tn}{tp + tn + fp + fn}. \quad (5)$$

The PA is defined as the number of correctly classified pixels over the total number of pixels. The IOUs and PAs of all classes (four classes exist in SPR, namely rivet, upper sheet, lower sheet, and background) were averaged (namely mIOU and mPA, respectively; ‘m’ denotes mean) and used for measuring material segmentation performance.

In Fig. 7, the mIOU-epoch curves for the training (black line) and validation datasets (blue line) are presented for the two successive training sessions (output stride = 16 in epochs 0–99 and 8 in epochs 100–199). The validation accuracy reached the maximum at epoch 157 (98.35%), so the model parameters at this epoch were used for testing the model (i.e. the model was validated at epoch 157). In the test phase, three types of test sets comprising center-cropped CFRP-GA590DP OM images of 300 × 400 pixels (test set 1), full-scale CFRP-GA590DP OM images of 480 × 640 pixels (test set 2), and SPFC590DP-Al5052 OM images of 300 × 400 pixels (test set 3) were used. Test set 2 (full-scale) was introduced to simply confirm the general performance of the segmentation model, and the material segmentation results for test sets 1 (center-cropped) and three were the data to be used in the next cross-section predictive model.

This was because, in the case of CFRP-GA590DP, there was no problem in measuring the head height even if only the center was predicted, as there was no flexion at both ends. However, in the case of SPFC590DP-Al5052, the flexion at both ends was large so the predictions had to be made till this area (see Figs. 9 and 10). The test results are presented as the segmentation results in Section IV-A.

The cross-section predictive model (scalar-to-seg generator) was trained on dual GTX 1080 Ti GPUs. The height and width of the convolutional weights were 4, and they were initialized from the Gaussian distribution with a standard deviation of 0.02 [32]. The training data were augmented through weak image transformation ($\times 50$) and flipping the images to the left and right ($\times 2$). The learning rate and lambda of the L2 weight decay were 3.162×10^{-7} and 10^{-6} , respectively, which were identified using Bayesian optimization [37], [38]. The batch size was 12 and the lambda in the generator objective was 100. For the CFRP-GA590DP combination, one test force was fixed, and the remaining eight punch forces were used for training. This process was repeated for all punch forces (29, 34, 39, 44, 49.8, 55, 60, 65, and 70 kN). Thus, training was performed over nine sessions. (The model was considered validated if all nine trained models made accurate predictions.) For the SPFC590DP-Al5052 sheets, all the data were divided into training, validation, and test sets, and four training sessions were performed as follows: a) using 40 kN as the validation set and 34 kN as the test set; b) 34 kN as the validation set and 40 kN as the test set; c) 43 kN as the validation set and 37 kN as the test set; d) 37 kN as the validation set and 43 kN as the test set. In each session, the remaining forces were used for training. In the testing phase, after completion of training, three fixed latent variables were input with the punch force so that three predictions were obtained. Adam [39] was adopted as the optimizer in both the segmentation and predictive deep-learning models.

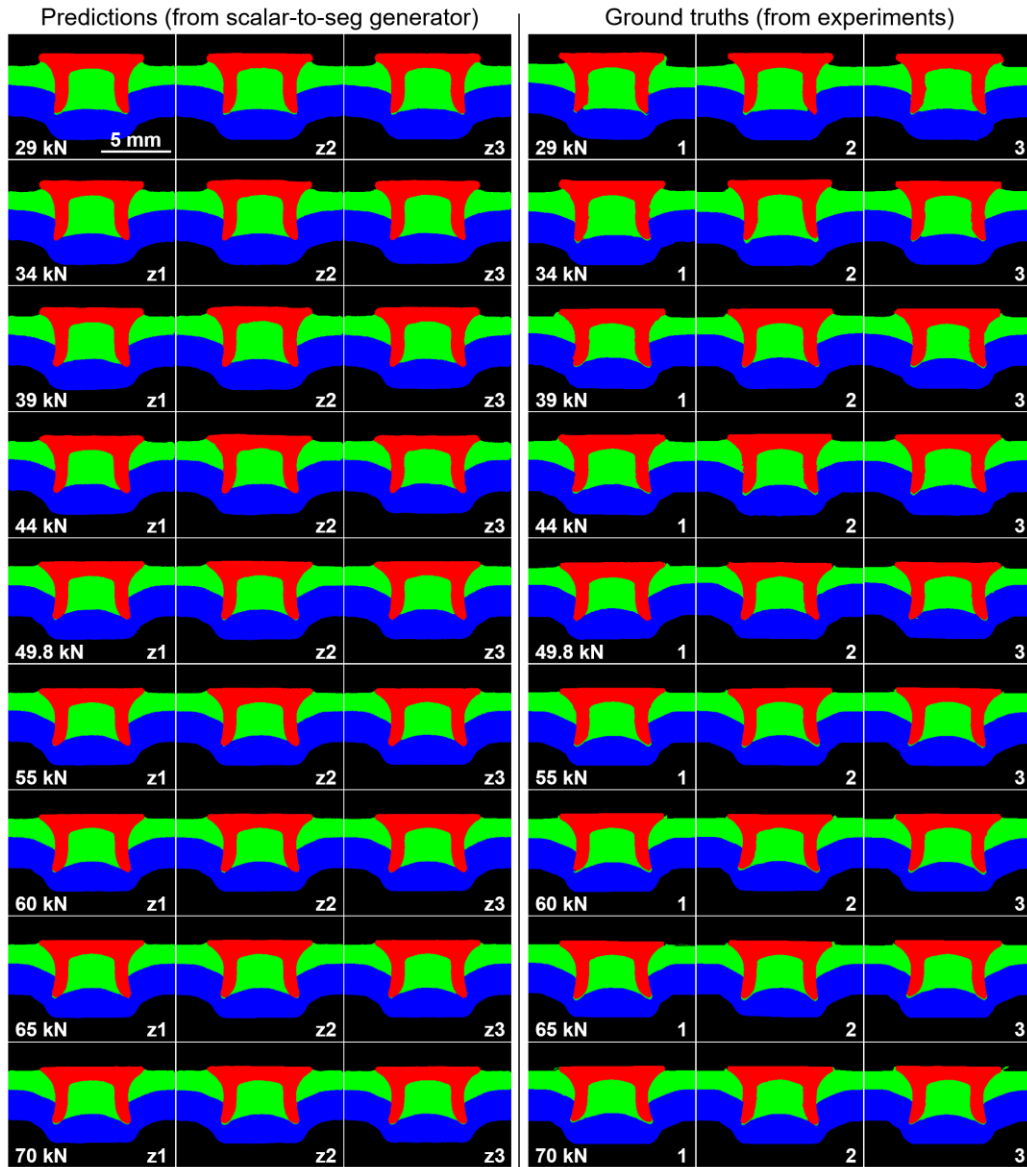


FIGURE 11. Prediction results (three columns on the left) and ground truths (three columns on the right) for the CFRP-GA590DP are presented for each punch force. The three columns of the prediction results represent three different generations from the scalar-to-seg generator according to three latent variables (z_1 , z_2 , z_3) marked at the bottom-right corner in each image. The three columns of the ground truths represent three repetitions of the SPR experiment and the repetition numbers (1, 2, 3) are mentioned at the bottom-right corner in each image. A scale bar is shown in the panel depicting the prediction for the punch force of 29 kN (z_1).

IV. RESULTS AND DISCUSSION

A. MATERIAL SEGMENTATION RESULT

Figs. 8, 9, and 10 present the material segmentation results for the three test sets. Each row in the figures corresponds to the OM inputs with punch forces of 44, 55, 65, and 70 kN for CFRP-GA590DP (Fig. 8 and Fig. 9) and 34, 40, and 43 kN for SPFC590DP-AI5052 (Fig. 10). The OM inputs, their ground truths (which were manually segmented by the authors), and AI prediction results are presented in the first, second, and third columns, respectively, and the last three columns are the segmentation images separated by channel (rivet, top sheet,

and bottom sheet classes), comprising the ground truths (top) and the predictions (bottom). The prediction accuracies indicated by mIOU and mPA are displayed at the bottom-right corner in each prediction map.

The figures indicate the successful performance of material segmentation in all the test sets. The accuracy reached 98–99%, which implies that the trained AI practically segmented the OM image in the same way as humans. Table 2 lists the IOU and PA accuracies for the three test sets according to class. The mean accuracy values for all classes and test sets were calculated as $mIOU = 98.50\%$ and

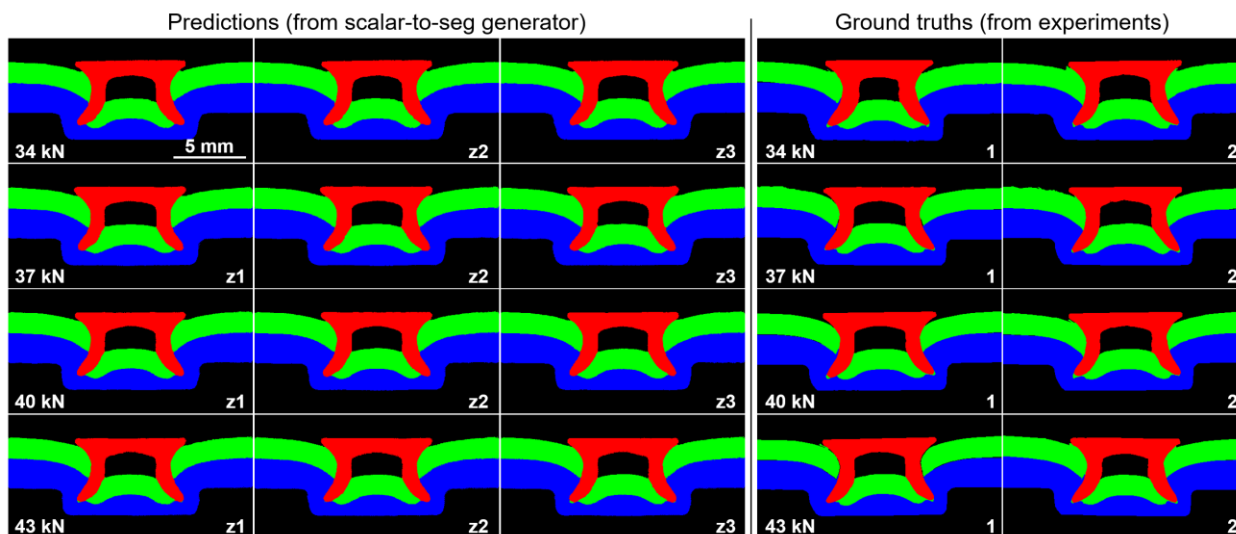


FIGURE 12. Prediction results (three columns on the left) and ground truths (two columns on the right) for SPFC590DP-A15052 are presented for each punch force. The three columns of the prediction results represent three different generations from the scalar-to-seg generator according to three latent variables (z_1 , z_2 , z_3) mentioned at the bottom-right corner in each image. The two columns of the ground truths represent two repetitions of the SPR experiment and the repetition numbers (1, 2) are mentioned at the bottom-right corner in each image. A scale bar is shown in the panel depicting the prediction for a punch force of 34 kN (z_1).

mPA = 99.78%. Moreover, as observed in Table 2, the mPAs for the three test sets are 99.75%, 99.83%, and 99.78%, which means that only 300 (0.25%), 522 (0.17%), and 264 (0.22%) pixels, respectively, were misclassified for the test sets when compared with the human segmentation results. These errors mostly originated from the ambiguity at the object boundaries, where the boundary itself contained multiple pixels instead of just one. For this reason, the PASCAL Visual Object Classes challenge [36] has the rule of discounting the border area of five pixels and regarding them as ‘void’ in the data to exclude the ambiguity when measuring the accuracies of the deep-learning models. This rule was not followed in this study because some interlock areas in the OM image were only a few pixels wide.

Furthermore, when trained with only CFRP-GA590DP data (excluding SPFC590DP-A15052 data), similar levels of testing accuracies could be reached using approximately two-thirds of the training epochs (mIOU = 98.49% and mPA = 99.77% when trained with an output stride of 16 for the first 50 epochs and eight for the next 50 epochs). This was an obvious result as the amount of to-be-trained information decreased (as observed in Figs. 9 and 10, there are several clear differences between the two sheet combinations, such as the existence of the hole just below the rivet). When training the model with both sheet combinations, 100 epochs were not enough, and at least 150 epochs were required, as mentioned in Section III-C.

After ensuring material segmentation with 98–99% accuracy, the training data to be used in the cross-section predictive model were safely replaced with the segmentation map, instead of the OM image. The cross-section predictive model can now be further trained by simply inputting new

OM images to the deep-learning segmentation model. Additionally, if other sheet combinations used in SPR are added in the future, the trained segmentation model can easily be trained further by restoring the parameters of the validated model.

B. CROSS-SECTIONAL SHAPE PREDICTION RESULT

Figs. 11 and 12 present the predicted material segmentation maps for each punch force in the three columns on the left (three latent variables), and their corresponding ground truths in the remaining columns on the right (repeated experiments). The random latent variables (z_1 , z_2 , z_3) and experiment repetition numbers (1, 2, 3 for CFRP-GA590DP and 1, 2 for SPFC590DP-A15052) are mentioned at the bottom-right corner of the images. The quality of the generated (predicted) images is high without any repeated, distorted, or blurred areas, owing to the modified structure and objective function. As seen in the predicted results in Fig. 11, the larger the punch force, the more the rivet is pressed and the greater is the interlock length. For a more accurate comparison with the ground truths, three geometrical key factors of head height, interlock, and bottom thickness were measured in every map and plotted versus the punch force in Figs. 13, 14, and 15, respectively (empty circle and square: CFRP-GA590DP; filled circle and square: SPFC590DP-A15052; black: ground truth; red: prediction). For each segmentation image, the three parameters were measured twice (on the left and right) and then averaged. As shown in Figs. 11 through 15, although slightly different cross-sections are generated under each punch force according to the introduced latent variables, the three important geometrical factors are properly mapped from the input punch force. Therefore, the generator was trained at a semantic

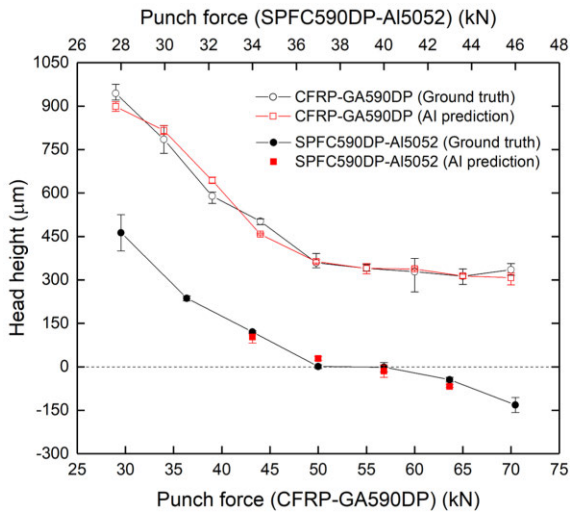


FIGURE 13. Head height measurements obtained from the AI predictions (red) and ground truths (black) according to the punch force (CFRP-GA590DP: left y-bottom x; SPFC590DP-AI5052: left y-top x).

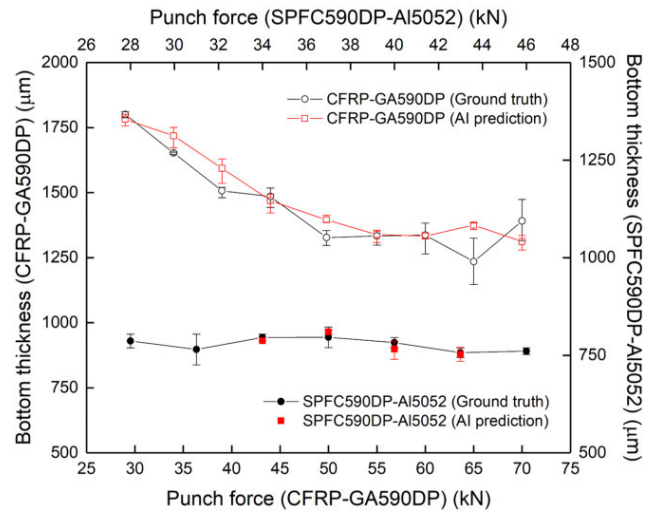


FIGURE 15. Results of the bottom thickness measurement from the AI prediction results (red) and the ground truths (black), according to the punch force (CFRP-GA590DP: left y-bottom x; SPFC590DP-AI5052: right y-top x).

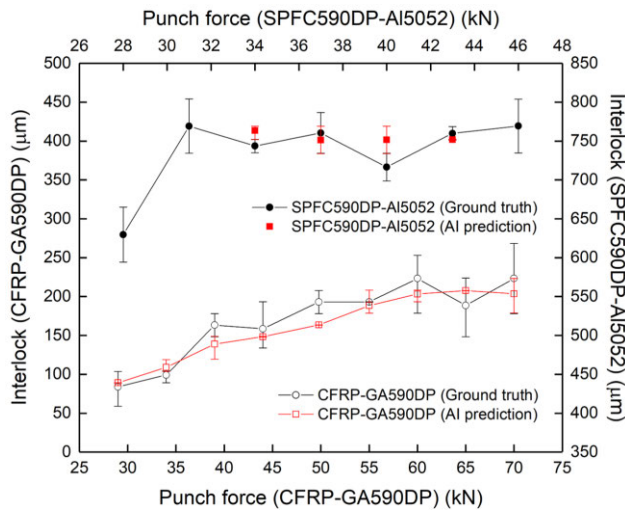


FIGURE 14. Interlock length measurements obtained from AI predictions (red) and ground truths (black) according to the punch force (CFRP-GA590DP: left y-bottom x; SPFC590DP-AI5052: right y-top x).

level by spontaneously grasping the relationship between the input punch forces and cross-sectional shapes, as the training proceeded. However, for the interlock length in SPFC590DP-AI5052 at 34–43 kN (see Fig. 14), the ground truth shows less tendency and so was the prediction result.

Tables 3 (for CFRP-GA590DP) and 4 (for SPFC590DP-AI5052) present the accuracies for the head height, interlock, length, and bottom thickness for each punch force. For the CFRP-GA590DP combination, the averaged accuracy across the punch forces for the head height, interlock length, and bottom thickness are 95.66%, 90.78%, and 96.16%, respectively, and for the SPFC590DP-AI5052 combination, the accuracies are 92.76%, 97.55%, and 98.60%, respectively.

For more intuitive comparison, Fig. 16(a) shows the AI-predicted CFRP-GA590DP cross-sectional shapes

TABLE 3. Calculated accuracies of the head height, interlock, and bottom thickness according to the punch force for the CFRP-GA590DP sheets.

Accuracy (%)	29 kN	34 kN	39 kN	44 kN	49.8 kN
Head height	95.24	96.06	90.91	91.22	98.94
Interlock	93.72	90.16	85.09	93.61	84.74
Bottom thickness	98.97	96.01	94.29	98.96	94.90
Accuracy (%)	55 kN	60 kN	65 kN	70 kN	Avg.
Head height	99.88	97.03	99.88	91.75	95.66
Interlock	97.59	91.11	89.83	91.18	90.78
Bottom thickness	99.64	99.74	88.62	94.32	96.16
Mean accuracy					94.20%

TABLE 4. Calculated accuracies of the head height, interlock, and bottom thickness according to the test punch force for the SPFC590DP-AI5052 sheets.

Accuracy (%)	34 kN	37 kN	40 kN	43 kN	Avg.
Head height	85.51	90.75	97.77	97.03	92.76
Interlock	97.34	98.78	95.12	98.95	97.55
Bottom thickness	98.95	98.22	97.88	99.37	98.60
Mean accuracy					96.31%

(left half) and the OM images obtained from the SPR experiments (right half) involving different punch forces (29, 39, 55, and 70 kN) alongside the measurement data. (Fig. 16(b): SPFC590DP-AI5052 for punch forces of 34, 40, and 43 kN) As seen, the region of each material segment

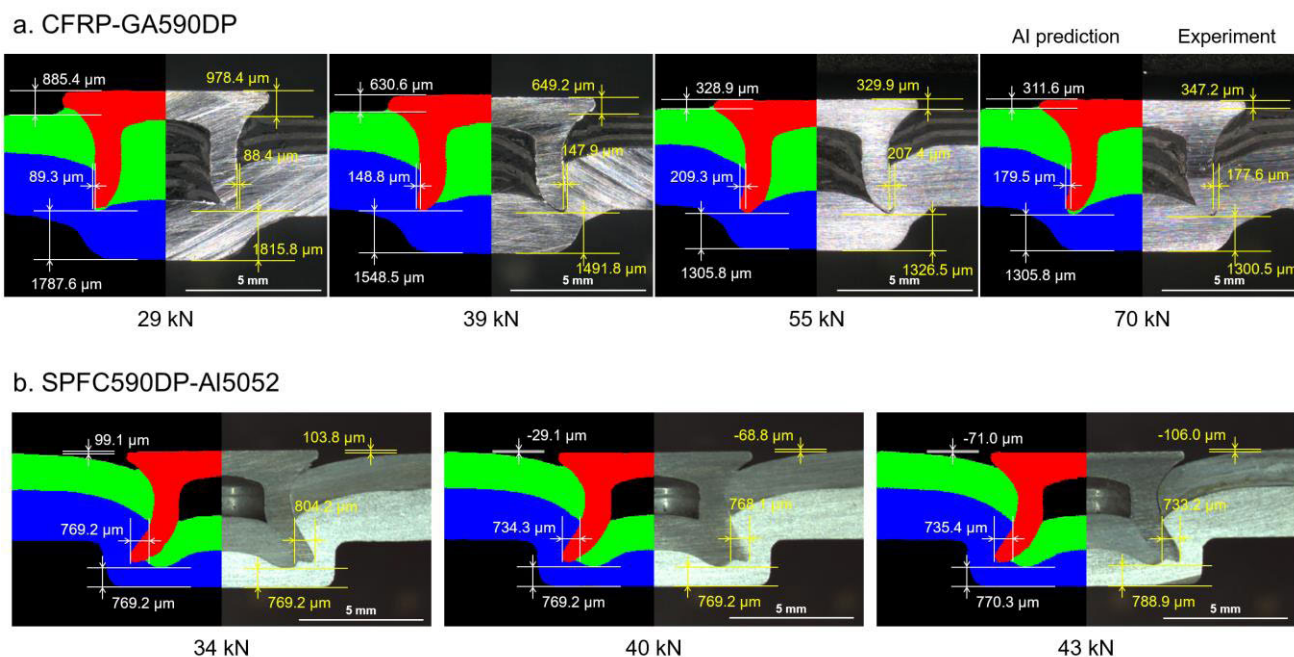


FIGURE 16. Comparison between AI-predicted results (left half) and OM images obtained experimentally (right half). (a) The punch forces used for CFRP-GA590DP were 29, 39, 55, and 70 kN. (b) The punch forces used for SPFC590DP-AI5052 were 34, 40, and 43 kN. These forces were applied in the experiments and provided as inputs to the deep-learning model as scalar values. The head height, interlock length, and bottom thickness are indicated in each figure.

in the AI-predicted results is almost identical to that of the OM images. The presented results suggest that the deep-learning architecture can be extremely useful in predicting the deformed cross-sectional shape in the SPR process.

V. CONCLUSIONS

We conducted a study for predicting the cross-sectional shapes in SPR of CFRP and GA590DP steel sheets and SPFC590DP and AI5052 sheets by applying state-of-the-art deep-learning algorithms. Two deep-learning architectures were trained for data characterization and prediction. The major findings can be summarized as follows:

- To characterize the cross-sectional shapes of the self-pierced specimens, the OM images obtained from the SPR experiment were segmented material by material by employing a CNN-based deep-learning architecture. We obtained mIOU and mPA values of 98.50% and 99.78%, respectively.

- Using the scalar punch force, the cross-sectional shape was predicted by a generative model based on CNN and cGAN architectures with residual blocks (scalar-to-seg generator). The cost function was modified considering the type of the ground truth (segmentation map). The proposed generator can produce segmentation images of considerably better quality.

- The accuracies of the cross-sectional shape predictions of the major geometrical factors in SPR, namely, the rivet head height, interlock length, and bottom thickness, were 95.66%, 90.78%, and 96.16%, respectively (mean 94.20%)

for CFRP-GA590DP, and 92.76%, 97.55%, and 98.60% (mean 96.31%) for SPFC590DP-AI5052, respectively.

REFERENCES

- [1] G. Di Franco, L. Fratini, A. Pasta, and V. F. Ruisi, "On the self-piercing riveting of aluminium blanks and carbon fibre composite panels," *Int. J. Mater. Forming*, vol. 6, no. 1, pp. 137–144, Mar. 2013, doi: 10.1007/s12289-011-1067-2.
- [2] X. Zhang, X. He, B. Xing, L. Zhao, Y. Lu, F. Gu, and A. Ball, "Influence of heat treatment on fatigue performances for self-piercing riveting similar and dissimilar titanium, aluminium and copper alloys," *Mater. Des.*, vol. 97, pp. 108–117, May 2016, doi: 10.1016/j.matdes.2016.02.075.
- [3] R. Haque, "Quality of self-piercing riveting (SPR) joints from cross-sectional perspective: A review," *Arch. Civil Mech. Eng.*, vol. 18, no. 1, pp. 83–93, Jan. 2018, doi: 10.1016/j.acme.2017.06.003.
- [4] R. Porcaro, A. G. Hanssen, M. Langseth, and A. Aalberg, "Self-piercing riveting process: An experimental and numerical investigation," *J. Mater. Process. Technol.*, vol. 171, no. 1, pp. 10–20, Jan. 2006, doi: 10.1016/j.jmatprotec.2005.05.048.
- [5] G. Casalino, A. Rotondo, and A. Ludovico, "On the numerical modelling of the multiphysics self piercing riveting process based on the finite element technique," *Adv. Eng. Softw.*, vol. 39, no. 9, pp. 787–795, Sep. 2008, doi: 10.1016/j.advengsoft.2007.12.002.
- [6] E. Atzeni, R. Ippolito, and L. Settineri, "Experimental and numerical appraisal of self-piercing riveting," *CIRP Ann.*, vol. 58, no. 1, pp. 17–20, 2009, doi: 10.1016/j.cirp.2009.03.081.
- [7] L. Huang, J. V. Lasecki, H. Guo, and X. Su, "Finite element modeling of dissimilar metal self-piercing riveting process," *SAE Int. J. Mater. Manuf.*, vol. 7, no. 3, pp. 698–705, Apr. 2014.
- [8] M. Carandente, R. J. Dashwood, I. G. Masters, and L. Han, "Improvements in numerical simulation of the SPR process using a thermo-mechanical finite element analysis," *J. Mater. Process. Technol.*, vol. 236, pp. 148–161, Oct. 2016, doi: 10.1016/j.jmatprotec.2016.05.001.
- [9] Y. W. Ma, Y. B. Li, W. Hu, M. Lou, and Z. Q. Lin, "Modeling of friction self-piercing riveting of aluminum to magnesium," *J. Manuf. Sci. Eng.*, vol. 138, no. 6, Jun. 2016, Art. no. 061007, doi: 10.1115/1.4032085.

- [10] F. Hönsch, J. Domitner, C. Sommitsch, B. Götzinger, and M. Közl, "Numerical simulation and experimental validation of self-piercing riveting (SPR) of 6xxx aluminium alloys for automotive applications," *J. Phys., Conf. Ser.*, vol. 1063, Jul. 2018, Art. no. 012081.
- [11] R. Haque, N. S. Williams, S. E. Blacket, and Y. Durandet, "A simple but effective model for characterizing SPR joints in steel sheet," *J. Mater. Process. Technol.*, vol. 223, pp. 225–231, Sep. 2015, doi: [10.1016/j.jmatprotec.2015.04.006](https://doi.org/10.1016/j.jmatprotec.2015.04.006).
- [12] L. Kroll, S. Mueller, R. Mauer mann, and R. Gruetzner, "Strength of self-piercing riveted joints for CFRP/aluminium sheets," in *Proc. 18th Int. Conf. Composite Mater. (ICCM)*, Seoul, South Korea, 2011, pp. 21–26.
- [13] F. Hirsch, S. Müller, M. Machens, R. Staschko, N. Fuchs, and M. Kästner, "Simulation of self-piercing rivetting processes in fibre reinforced polymers: Material modelling and parameter identification," *J. Mater. Process. Technol.*, vol. 241, pp. 164–177, Mar. 2017, doi: [10.1016/j.jmatprotec.2016.10.010](https://doi.org/10.1016/j.jmatprotec.2016.10.010).
- [14] Y. Lecun, L. Bottou, Y. Bengio, and P. Haffner, "Gradient-based learning applied to document recognition," *Proc. IEEE*, vol. 86, no. 11, pp. 2278–2324, Nov. 1998, doi: [10.1109/5.726791](https://doi.org/10.1109/5.726791).
- [15] G. E. Hinton, "Reducing the dimensionality of data with neural networks," *Science*, vol. 313, no. 5786, pp. 504–507, Jul. 2006, doi: [10.1126/science.1127647](https://doi.org/10.1126/science.1127647).
- [16] L.-C. Chen, Y. Zhu, G. Papandreou, F. Schroff, and H. Adam, "Encoder-decoder with atrous separable convolution for semantic image segmentation," in *Proc. Eur. Conf. Comput. Vis. (ECCV)*, 2018, pp. 801–818.
- [17] I. Goodfellow, J. Pouget-Abadie, M. Mirza, B. Xu, D. Warde-Farley, S. Ozair, A. Courville, and Y. Bengio, "Generative adversarial nets," in *Proc. Adv. Neural Inf. Process. Syst.*, vol. 27, 2014, pp. 2672–2680.
- [18] M. Mirza and S. Osindero, "Conditional generative adversarial nets," 2014, *arXiv:1411.1784*. [Online]. Available: <http://arxiv.org/abs/1411.1784>
- [19] K. He, X. Zhang, S. Ren, and J. Sun, "Deep residual learning for image recognition," in *Proc. IEEE Conf. Comput. Vis. Pattern Recognit.*, Jun. 2016, pp. 770–778.
- [20] S. Gross and M. Wilber. (2016). *Training and Investigating Residual Nets*. [Online]. Available: <http://torch.ch/blog/2016/02/04/resnets.html>
- [21] F. Chollet, "Xception: Deep learning with depthwise separable convolutions," in *Proc. IEEE Conf. Comput. Vis. Pattern Recognit.*, Jun. 2017, pp. 1251–1258.
- [22] O. Ronneberger, P. Fischer, and T. Brox, "U-net: Convolutional networks for biomedical image segmentation," in *Proc. MICCAI*, 2015, pp. 234–241.
- [23] C. Ledig, L. Theis, F. Huszar, J. Caballero, A. Cunningham, A. Acosta, A. Aitken, A. Tejani, J. Totz, Z. Wang, and W. Shi, "Photo-realistic single image super-resolution using a generative adversarial network," in *Proc. IEEE Conf. Comput. Vis. Pattern Recognit. (CVPR)*, Jul. 2017, pp. 4681–4690.
- [24] T.-C. Wang, M.-Y. Liu, J.-Y. Zhu, A. Tao, J. Kautz, and B. Catanzaro, "High-resolution image synthesis and semantic manipulation with conditional GANs," in *Proc. IEEE Conf. Comput. Vis. Pattern Recognit.*, Jun. 2018, pp. 8798–8807.
- [25] Y. Zhang, Y. Tian, Y. Kong, B. Zhong, and Y. Fu, "Residual dense network for image super-resolution," in *Proc. IEEE Conf. Comput. Vis. Pattern Recognit.*, Jun. 2018, pp. 2472–2481.
- [26] X. Wang, K. Yu, S. Wu, J. Gu, Y. Liu, C. Dong, Y. Qiao, and C. C. Loy, "ESRGAN: Enhanced super-resolution generative adversarial networks," in *Proc. Eur. Conf. Comput. Vis.* Springer, 2018, pp. 63–79.
- [27] T. Dai, J. Cai, Y. Zhang, S.-T. Xia, and L. Zhang, "Second-order attention network for single image super-resolution," in *Proc. IEEE Conf. Comput. Vis. Pattern Recognit. (CVPR)*, Jun. 2019, pp. 11065–11074.
- [28] S. Ioffe and C. Szegedy, "Batch normalization: Accelerating deep network training by reducing internal covariate shift," 2015, *arXiv:1502.03167*. [Online]. Available: <http://arxiv.org/abs/1502.03167>
- [29] D. Ulyanov, A. Vedaldi, and V. Lempitsky, "Instance normalization: The missing ingredient for fast stylization," 2016, *arXiv:1607.08022*. [Online]. Available: <http://arxiv.org/abs/1607.08022>
- [30] V. Nair and G. E. Hinton, "Rectified linear units improve restricted Boltzmann machines," in *Proc. 27th Int. Conf. Mach. Learn.*, 2010, pp. 807–814.
- [31] A. L. Maas, A. Y. Hannun, and A. Y. Ng, "Rectifier nonlinearities improve neural network acoustic models," in *Proc. ICML*, 2013, vol. 30, no. 1, p. 3.
- [32] A. Radford, L. Metz, and S. Chintala, "Unsupervised representation learning with deep convolutional generative adversarial networks," 2015, *arXiv:1511.06434*. [Online]. Available: <http://arxiv.org/abs/1511.06434>
- [33] P. Isola, J.-Y. Zhu, T. Zhou, and A. A. Efros, "Image-to-image translation with conditional adversarial networks," in *Proc. IEEE Conf. Comput. Vis. Pattern Recognit. (CVPR)*, Jul. 2017, pp. 1125–1134.
- [34] D. Pathak, P. Krahenbuhl, J. Donahue, T. Darrell, and A. A. Efros, "Context encoders: Feature learning by inpainting," in *Proc. IEEE Conf. Comput. Vis. Pattern Recognit. (CVPR)*, Jun. 2016, pp. 2536–2544.
- [35] X. Mao, Q. Li, H. Xie, R. Y. K. Lau, Z. Wang, and S. P. Smolley, "Least squares generative adversarial networks," in *Proc. IEEE Int. Conf. Comput. Vis. (ICCV)*, Oct. 2017, pp. 2794–2802.
- [36] M. Everingham, L. Van Gool, C. K. I. Williams, J. Winn, and A. Zisserman, "The Pascal visual object classes (VOC) challenge," *Int. J. Comput. Vis.*, vol. 88, no. 2, pp. 303–338, Jun. 2010.
- [37] E. Brochu, V. M. Cora, and N. de Freitas, "A tutorial on Bayesian optimization of expensive cost functions, with application to active user modeling and hierarchical reinforcement learning," 2010, *arXiv:1012.2599*. [Online]. Available: <http://arxiv.org/abs/1012.2599>
- [38] J. Snoek, H. Larochelle, and R. P. Adams, "Practical Bayesian optimization of machine learning algorithms," in *Proc. Adv. Neural Inf. Process. Syst.*, 2012, pp. 2951–2959.
- [39] D. P. Kingma and J. Ba, "Adam: A method for stochastic optimization," 2014, *arXiv:1412.6980*. [Online]. Available: <http://arxiv.org/abs/1412.6980>



SEHYEOK OH received the B.S. degree in mechanical engineering from the Ulsan National Institute of Science and Technology (UNIST), Ulsan, South Korea, in 2014, where he is currently pursuing the combined M.S. and Ph.D. degree in mechanical engineering. His research interests include application of deep learning to the laser materials processing and mechanical engineering, and industrial application of high-power lasers, such as laser welding, laser cutting, and laser transformation hardening.



HYUN KYUNG KIM received the B.S. degree in mechanical engineering from the Ulsan National Institute of Science and Technology (UNIST), Ulsan, South Korea, in 2020, where she is currently pursuing the combined M.S. and Ph.D. degree in mechanical engineering. Her research interests include application of deep learning in laser processing and mechanical engineering.



TAEK-EON JEONG received the B.S. degree in mechanical engineering from Myoungji University, Seoul, South Korea, in 2018, and the M.S. degree in mechanical convergence engineering from Hanyang University, Seoul, in 2020.

From 2018 to 2020, he was a Research Assistant with the Joining Research and Development Group, Korea Institute of Industrial Technology, South Korea. His research interests include mechanical joining of dissimilar materials and laser surface treatment to improve the strength of adhesive bonding and laser fusion bonding.

Mr. Jeong has won three awards of Excellent Paper Presentation at the Korean Welding and Joining Society.



DONG-HYUCK KAM received the B.S. degree in mechanical engineering from the Pohang University of Science and Technology, Pohang, South Korea, in 2003, and the M.S.E. and Ph.D. degrees in mechanical engineering from the University of Michigan, Ann Arbor, USA, in 2005 and 2009, respectively.

From 2011 to 2015, he was a Senior Engineer with Samsung Electronics Company Ltd. Since 2015, he has been a Principal Researcher with the Joining Research and Development Group, Korea Institute of Industrial Technology. His research interests include mechanical joining of dissimilar materials, hybrid welding of zinc coated steel, laser-based joining technologies for CFRP-metal, 3D metal deposition with wire feeding, and laser material processing.



HYUNGSON KI received the B.S. degree in mechanical engineering from the Pohang University of Science and Technology (POSTECH), South Korea, in 1996, and the M.S. and Ph.D. degrees in mechanical engineering from the University of Michigan, Ann Arbor, in 1998 and 2001, respectively.

From 2001 to 2003, he was a Postdoctoral Research Fellow with the University of Michigan. From 2003 to 2008, he was an Assistant Professor of mechanical engineering with Michigan State University, East Lansing, MI, USA. He is currently a Professor in mechanical engineering with the Ulsan National Institute of Science and Technology (UNIST), South Korea. His research interests include laser material interaction and processing, multiphysics simulations, and deep-learning applications.

• • •